Metallurgical and Materials Transactions A manuscript No.
(will be inserted by the editor)

Crystallography, Morphology, and Martensite Transformation of Prior Austenite in Intercritically Annealed High-Aluminum Steel

T. Nyyssönen · P. Peura · V.-T. Kuokkala

Received: date / Accepted: date

This is a post-peer-review, pre-copyedit version of an article published in Metallurgical and Materials Transactions A. The final authenticated version is available online at: http://dx.doi.org/10.1007/s11661-018-4904-9

Abstract The crystallography and morphology of the intercritical austenite phase in two high-aluminum steels annealed at 850 °C was examined on the basis of electron backscattered diffraction analysis, in concert with a novel orientation relationship determination and prior austenite reconstruction algorithm. The formed intercritical austenite predominantly shared a Kurdjumov-Sachs type semicoherent boundary with at least one of the neighboring intercritical ferrite grains. If the austenite had nucleated at a high-energy site (such as a grain corner or edge), no orientation relationship was usually observed. The growth rate of the austenite grains was observed to be slow, causing phase inequilibrium even after extended

T. Nyyssönen · P. Peura · V.-T. Kuokkala

Department of Materials Science, Tampere Univ. of Technology, P.O. Box 589, 33101 Tampere, Finland

T. Nyyssönen

Tel.: +358408490138

E-mail: tuomo.nyyssonen@tut.fi

annealing times. The small austenite grain size and phase fraction were consequently shown to affect martensite start temperature. Both steels had distinct variant pairing tendencies in the intercritically annealed condition.

Keywords Ferrite · Austenite · Martensite · Orientation relationship · EBSD

1 Introduction

Low-alloy dual-phase (hereafter referred to as DP) steels are characterized by a microstructure consisting of fine recrystallized ferrite with evenly dispersed islands of martensite. This structure is typically developed by the annealing of a cold-rolled ferrite-pearlite microstructure at a temperature between A_{c1} and A_{c3}, followed by quenching to room temperature in a continuous annealing line. The phase fractions, morphology, and the crystallographic texture of the final DP product are inherited from the cold-rolled structure through ferrite recrystallization, austenite nucleation and growth, and finally martensitic transformation.

The focus of this paper is on the nucleation and growth of austenite during intercritical annealing, with an emphasis on its morphology and crystallographic properties. Dilatometry heat treatments were carried out for two high-aluminum steels, followed by electron backscattered diffraction (hereafter referred to as EBSD) analysis.

The contributions in this paper are as follows. It is shown that Markov clustering [1] combined with the iterative determination of the austenite-martensite orientation relationship (hereafter referred to as OR) [2] can be used to reconstruct the EBSD orientation map of austenite formed during intercritical annealing. The algorithm used for this purpose is described and made freely available. The accuracy of the OR determined from martensitic lath boundaries with the iterative method is discussed and compared with the OR observed directly between martensite and reconstructed austenite. Based on the reconstructed image maps and op-

tical microscopy, the growth mechanisms prevalent in two intercritically annealed high-aluminum steels are identified, as well as the significant aspects affecting the martensite start temperatures determined through dilatometry. It is shown how the various ORs determined in this work deviate from the Kurdjumov-Sachs [3] orientation relationship.

2 Intercritical austenite morphology and crystallography

It has previously been reported by Garcia and DeArdo [4] that in a cold-rolled, 1.5 wt-% Mn steel, austenite preferentially nucleates at cementite particles on ferrite-ferrite grain boundaries. In various studies, the austenite grains have often been observed to bear a Kurdjumov-Sachs type orientation relationship with a neighboring ferrite grain [5,6,7]. Shtansky et al. [5] reported that the growth direction of a nucleated austenite grain is then towards an adjacent neighbor with an incoherent phase boundary, which has greater mobility compared to an ordered, semicoherent interface. Austenite growth is initially rapid [4,5], controlled primarily by the diffusion of carbon, but at later stages slows down as interstitial alloying elements start to partition between the phases.

While various studies have been carried out over the years to determine the kinetics of austenite formation in DP steels [4,5,8,9,10,11], crystallographic analysis of the austenite phase has been less common. The cited studies have concerned the analysis of retained austenite either through EBSD [6] or transmission electron microscopy studies [5,11]. These methods cannot be applied to the study of ferrite-martensite dual phase steels directly, because austenite is either completely absent or present in such small amounts that statistical analysis of the results is not worthwhile. One way to mitigate this issue is the reconstruction of prior austenite orientation maps from EBSD orientation maps. Several approaches for prior austenite reconstruction have been created over the last few years [12,13,14,

15, 16].

The current reconstruction methods can be broadly divided into two categories: operations on a weighted graph constructed from a grain map [12, 14] and operations on cropped sections of the orientation map that has been segmented into a square grid [16, 13]. In both approaches, the goal is to identify a suitable amount of crystallographically distinct martensitic variant orientations originating from the same prior austenite grain, for which a reliable estimation of a prior austenite orientation can be made. A growth or link-up procedure for these initial variant clusters is usually included in the method [12, 15, 16] to reconstruct prior austenite grains fully. The grain map approach is computationally efficient, reducing the number of orientations necessary to process. On the other hand, Bernier et al. [16] and Miyamoto et al. [13] claim that reconstruction on a local, pixel-based scale allows for more reliable reconstruction results for deformed austenite grains with orientation gradients.

One of the main problems in the reconstruction of prior austenite orientation maps is the high frequency of ambiguous variant orientations that are crystallographically related to several neighboring prior austenite orientations [14]. Prior austenite orientations may share one or more variants as a random occurrence, caused by the high degree of symmetricity in the cubic lattices involved in the phase transformations. However, it is a more likely event that a prior austenite grain has one or more $\Sigma 3$ type twins, resulting in six martensite variant orientations shared by each twin when the transformation follows the Kurdjumov-Sachs orientation relationship [14]. For these reasons, misidentified austenite orientations are a common occurrence at prior austenite grain boundaries and twin orientations especially may be frequently misidentified during reconstruction.

The methods discussed here require an assumption about the austenite-martensite orientation relationship (OR), which is the misorientation necessary to bring an orientation in the austenite coordinate system to the martensite coordinate system. Several authors [13, 14, 16] have found that the use of an experimentally measured OR results in improved reconstruction performance, considerably reducing ambiguous variant orientations and improving twin identification. Bernier et al. [16] and Miyamoto et al. [13] determined an optimal OR through a manual grain selection method followed by numerical fitting. Humbert et al. [17] also performed such an analysis for a manually cropped prior austenite grain. In this case, the approach for OR determination was based on finding the correct symmetry operators resulting in a common parent austenite orientation. Later, Humbert et al. [18] presented a modification where the OR was determined through the analysis of triple junctions of martensitic variants inherited from the same parent grain. Although not discussed in the article, the calculations suggest that this approach should also be viable for cases where the dataset selected for OR refinement contains martensitic orientations from several prior austenite grains. It bears mentioning that the OR determined in this manner is an average value, and in reality varies considerably depending on local conditions. Cayron et al. [19] observed considerable variation in the orientation relationship between austenite and martensite even within individual prior austenite grains.

In the case of DP steels, the size of prior austenite grains is relatively small, on the order of a few μm. The small parent austenite grain size will significantly reduce the available data for the determination of the optimal OR with a manual selection method, so its use is not practical. In the present study, an algorithm was created for the automatic reconstruction of local austenite orientations that addresses this issue. The austenite reconstruction algorithm presented here consists of three major steps. The first step is the determination of the orientation relationship from intergranular misorientations as per the procedure outlined in [2]. The

second step is the construction of an undirected graph G describing the EBSD grain map, in which each individual grain represents a node and the neighbor-to-neighbor misorientations represent edges connecting the nodes. The third and final step is the separation of discrete clusters (prior austenite grains) from the undirected graph with the use of the Markov Cluster Algorithm (hereafter referred to as MCL [1,20]).

MCL is meant for discovering natural groups (or clusters) in graphs, postulating that a random walk in an undirected graph G that visits a dense natural group is unlikely to leave before visiting the nodes in that group many times. With a series of mathematical operations, the connections within the natural groups are strengthened and the connections between groups weakened, with the final result being a group of distinct clusters. Here, the expected natural groups in G are defined by parent austenite grains. Each node within a group originating from a single parent austenite grain will have many strong connections with the other nodes of the same group, while the connections to nodes from other groups (other parent austenite grains) will be sparse and weak. The algorithm is computationally efficient and does not require the specification of a predefined number of clusters. Previously, Gomes and Kestens [20] showed succesful austenite reconstructions produced via the MCL route, although they did not provide details of their algorithm. A full description of MCL can be found in the dissertation of Van Dongen [1]. Here, the focus is on how the Markov matrix T_{G+I} was assembled using the iterative OR determination algorithm [2] and what operations it was subjected to during the reconstruction.

The described method is largely similar to the one proposed by Gomes and Kestens [20], with the major difference being the iterative algorithm used to determine an experimentally observed orientation relationship. It has some similarities to the methods by Cayron et al. [12] and Germain et al. [14], in that operations

are conducted on a weighted graph constructed from a grain map. The main difference compared to these two methods is the attempt here to segment the graph into clusters before the calculation of prior orientations. From a computational perspective, this will reduce the number of calculations necessary to determine parent orientations. The downside is the lack of information concerning ambiguous prior orientations, which can be better identified if the prior orientation of an individual node is considered for multiple clusters [14].

3 Calculation

In this section, the algorithm for the reconstruction of parent austenite orientation maps is described.

3.1 Step 1: Orientation relationship determination

The crystallographic orientation of martensite at a point x_i on a suitably prepared surface can be determined by means of electron backscattered diffraction in a scanning electron microscope. This martensitic orientation can be thought of as the result of a specific rotation of a previous orientation in the coordinate system of a prior austenite phase. The orientation relationship between the prior austenite and martensite orientations can then be expressed in the following manner:

$$O_{\alpha'}(x_i) = O_{\gamma}(x_i) P_i T_{\gamma \to \alpha} C_i \tag{1}$$

In Equation 1, O_{γ} and $O_{\alpha'}$ are orientation matrices representing the crystallographic orientations of austenite and martensite at x_i. $T_{\gamma \to \alpha}$ is a misorientation matrix representing the orientation relationship between the phases. P_i is one of 24 rotational symmetry operators for the prior austenite phase and C_i is a corresponding symmetry operator for the martensite phase. Considering all combinations of symmetry operators, the equation results in 24 distinct $O_{\alpha'}$ variant orientations

for the same O_γ when calculated using the Kurdjumov-Sachs OR. Further assuming that neighboring orientation measurements at locations x_i and x_j represent two different martensitic variants that have been formed from the same austenitic parent grain, the misorientation matrix M between the two would be:

$$M = C_j^{-1} T_{\gamma\to\alpha}^{-1} P_j^{-1} P_i T_{\gamma\to\alpha} C_i \tag{2}$$

It can be found that $T_{\gamma\to\alpha}^{-1} P_j^{-1} P_i T_{\gamma\to\alpha}$ results in multiple occupations of some rotations and can be fully described with a set of 24 distinct solutions, in the case of the Kurdjumov-Sachs and various other ORs, as remarked by various authors [13,21,22,23]. Considering only the combinations of C_i and C_j, each singular misorientation has 24^2 crystallographically related solutions.

To determine whether an experimentally observed misorientation M_{exp} between points x_i and x_j can be described with Equation 2, it is necessary to calculate its deviation angle with each possible candidate M, resulting in 24^3 comparisons to a single M_{exp}. If the smallest deviation angle found from this set of comparisons falls below a predetermined threshold value, the experimentally observed misorientation can be classified as a misorientation between two laths originating from the same prior austenite grain.

Prior to this calculation, it is necessary to determine an initial candidate for $T_{\gamma\to\alpha}$, such as the orientation relationship determined by Kurdjumov and Sachs. The K-S OR predicts that the $(111)\gamma$ and $(011)\alpha'$ planes and the $[\bar{1}01]\gamma$ and $[\overline{11}1]\alpha'$ directions are exactly parallel. Studies by Miyamoto et al. [13] and Stormvinter et al. [22] have shown that actually observed orientation relationships differ considerably from the K-S OR and that it is necessary to determine an experimentally obtained average value for the orientation relationship to ensure a reliable indexation of the symmetry operators necessary to properly characterize

each experimentally observed misorientation.

To this end, solving for $T_{\gamma\to\alpha}$ by manipulating Equation 2 gives:

$$T_{\gamma\to\alpha} = (T^{-1}_{\gamma\to\alpha} P_j^{-1} P_i)^{-} 1 C_j M_{exp} C_i^{-} 1 \tag{3}$$

Unfortunately, $T_{\gamma\to\alpha}$ is found on both sides of the equation, so it cannot be solved directly using Equation 3. Instead, an assumption $T_{\gamma\to\alpha} = T_{\gamma\to\alpha,init.}$ must be made to obtain $T_{\gamma\to\alpha}$. An erroneous assumption of $T_{\gamma\to\alpha,init.}$ will result in a misorientation between the true orientation relationship and the calculated $T_{\gamma\to\alpha}$. However, assuming that in a large set of misorientations where all combinations of symmetry operators are equally represented, the mean of the $T_{\gamma\to\alpha}$ determined in this manner will equal the true orientation relationship. This is visualized in Figure 1, in which the OR is shown as $(011)\alpha'$ and $[\overline{1}\overline{1}1]\alpha'$ orientations on a standard stereographic projection for austenite. In the Figure, the K-S OR has been taken as the assumed orientation relationship $T_{\gamma\to\alpha,init.}$ and the misorientation matrix M_{exp} has been created with the Greninger-Troiano OR, using Equation 2. Identity matrices were taken as C_i and C_j, resulting in 24 misorientations in

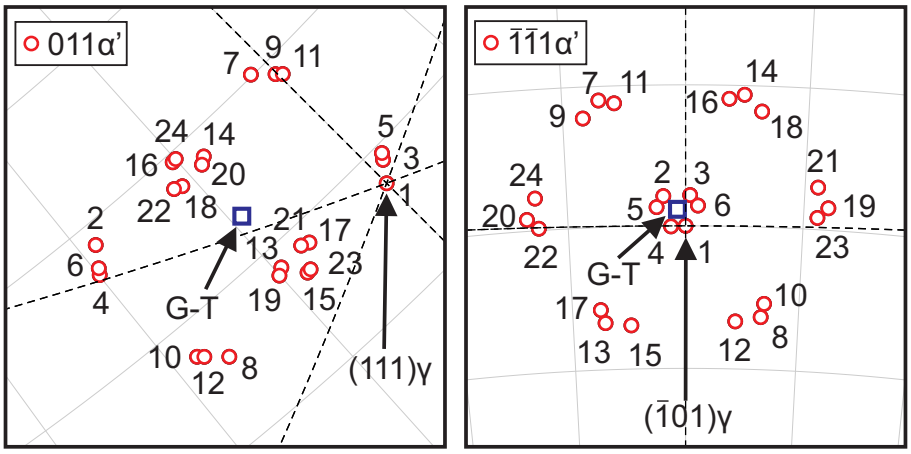

Fig. 1 Sections of a standard stereographic projection for austenite, overlaid with corresponding a) $(011)\alpha'$ planes and b) $[\overline{1}\overline{1}1]\alpha'$ directions. The grid spacing in the figure is 3 degrees.

M_{exp}. The G-T relationship corresponds exactly with the mean of the orientation relationships calculated with Equation 3.

An iterative procedure can therefore be used for the determination of the true OR:

$$T_{n+1}(x_i, x_j) = (\overline{T}_n^{-1} P_j^{-1} P_i)^{-1} C_j M_{x_i,x_j} C_i^- 1 \tag{4}$$

In Equation 4, $T_{n+1}(x_i, x_j)$ is an austenite-martensite orientation relationship resulting from n+1 iterations, determined from the misorientation M_{x_i,x_j}, which is the misorientation between experimentally determined orientations $O_{\alpha'}(x_i)$ and $O_{\alpha'}(x_j)$. $T_{n+1}(x_i, x_j)$ is calculated using the symmetry operators C_i and C_j and the inverse austenite-martensite orientation relationship described by $\overline{T}_n^{-1} P_j^{-1} P_i$. The symmetry operators have been determined with Equation 2, assuming $T_{\gamma\to\alpha} = \overline{T}_n$, by comparison of all possible calculated misorientations to observed M_{x_i,x_j}. $\overline{T}_n$ is the mean of all of the orientation relationships determined during the previous round of iteration.

The iterative procedure is based on the correct indexation of symmetry operators C_i and C_j and the identification of the correct $\overline{T}_n^{-1} P_j^{-1} P_i$. Several misindexations are likely to occur during the initial rounds of iteration, with indexation accuracy improving on each subsequent iteration round. When the indexation accuracy ceases to improve (or there is no change in the indexation of symmetry operators from one round of iteration to the next), the final $\overline{T}_n$ can be taken as the experimentally determined orientation relationship, $T_{\gamma\to\alpha}^{exp}$.

3.2 Step 2: Assembling the undirected graph

After many iterations, the indexation of the symmetry operators does not improve further. The final $\overline{T}_n$ can then be taken as $T^{exp}_{\gamma\rightarrow\alpha}$ and it can be used to generate a list of theoretical misorientations, to which the list of experimentally measured intergranular misorientations can be compared. Each intergranular misorientation M can then be assigned a value determining the likelihood to be a misorientation between two martensite grains originating from the same prior austenite grain. In this study the likelihood, with values ranging from 0 to 1, was determined using the Burr cumulative distribution survival function:

$$S(x|\alpha,c,k) = \frac{1}{[1+(\frac{M_{ang}}{\alpha})^c]^k} \tag{5}$$

where M_{ang} is the minimum deviation angle found between a given intergranular misorientation M and the theoretically generated set of martensitic misorientations. The constants α, c and k are scale and shape parameters with values of 2, 5 and 1, respectively. An m-by-m incidence matrix G can then be generated, in which m equals the total number of grains in the grain map and each individual element $e_{i,j}$ describes the edge $e = S_{i,j}$ between nodes (grains) i and j. The matrix is symmetric, with diagonal elements set to 1.

3.3 Step 3: Clusterization of the graph using MCL

Each column of the incidence matrix G is normalized by multiplying with a suitable diagonal matrix:

$$T_{G+I} = Gd_n \tag{6}$$

The resulting stochastic matrix $Q = T_{G+I}$ is then subjected to operations of expansion and inflation. Expansion consists simply of the multiplication of the stochastic matrix $Q = T_{G+I}$ by itself:

$$Q^2 = QQ \tag{7}$$

Inflation consists of a Hadamard (elementwise) power of r over Q^2 and is followed by the normalization of each column by multiplying the matrix with a suitable diagonal matrix d_t:

$$T_{G+I,2} = (Q^2)^{\circ r} d_t \tag{8}$$

where $\circ r$ denotes the Hadamard power. The result is another stochastic matrix, in which the edges of nodes within clusters are strengthened and the node edges between the clusters are weakened. After a sufficient amount of alternating sets of expansion and inflation, the intercluster edges become zero and the resulting graph describes a set of discrete clusters. The process can be made more efficient by pruning the matrix during each inflation step prior to normalization. In the pruning process, edges that fall below a certain threshold are set to zero.

4 Materials and Methods

For the purposes of testing the reconstruction algorithm on a fully austenitized microstructure, a reference steel was heated to 1200 °C at 5 °C/s, soaked for three minutes and quenched to room temperature at 50 °C/s using a TA DIL805 dilatometer.

Two high-aluminum steels with nominal 0.2 wt-% carbon content were prepared for the intercritical austenite studies (hereafter referred to as steels A and B). Table 1 shows the steel compositions. The steels were vacuum-cast as 40x40x180

Table 1 Chemical compositions of the investigated steels.

Element [wt-%]	C	Mn	Si	Al	P	Ni	Cu	Nb	Cr
Steel A	0.19	1.99	0.38	1.96	0.05	0.02	0.02	0.03	0.11
Steel B	0.22	2.03	0.04	2.93	0.01	0.48	0.96	0.03	0.12

mm billets into a water-cooled copper die in a low pressure casting furnace. The cast specimens were soaked at 1200 °C for 30 minutes prior to hot and cold rolling into sheets using a laboratory rolling mill. The samples were first hot rolled into 3 mm sheets with the finish rolling temperature well above the recrystallization limit temperature, then quenched to 600 °C, followed by slow cooling by wrapping the hot rolled samples into an insulator blanket to simulate the cooldown after coiling. The specimens were subsequently cold rolled into 60 mm wide and 1.3 mm thick strips, from which 4x10 mm dilatometry specimens were cut.

The dilatometry specimens were then heat treated to produce a range of inter-critical annealing conditions, using a TA DIL805 dilatometer to assure a controlled heating and cooling cycle and for monitoring the dilatation of the specimens. The annealing temperatures were 750, 800, 850 and 900 °C with a heating rate of 5 °C/s, followed by annealing for varying holding times of 3, 10 and 60 minutes. At 900 °C, only the three minute holding time was studied. After annealing, the steels were quenched to room temperature at a cooling rate of 25 °C/s. A prediction for the balance of phases at thermodynamic equilibrium was calculated for each of the annealing conditions using the JMATPRO® [24] computer program. The predicted chemical composition of the equilibrium austenite phase fraction at each temperature was also calculated, as well as the predicted martensite start temperature (hereafter referred to as M_s) using the methodology outlined by Bhadeshia [25]. Table 2 shows the calculation results.

M_s temperatures were determined experimentally from the dilatometric data by least squares fitting of the Koistinen-Marburger equation [26] in the manner de-

Table 2 Calculated austenite fractions, M_s temperatures, and selected austenite phase constituents (in wt-%) at indicated annealing temperatures.

Steel	T_a, [°C]	f_γ	M_s, [°C]	C	Mn	Si	Al
A	750	0.24	82.83	0.77	4.09	0.32	1.57
	800	0.31	203.5	0.59	3.35	0.33	1.61
	850	0.40	285.8	0.46	2.88	0.34	1.67
	900	0.52	344.6	0.36	2.55	0.34	1.74
B	750	0.26	136.9	0.72	3.91	-	2.58
	800	0.33	240.9	0.57	3.25	-	2.61
	850	0.42	314.1	0.45	2.82	-	2.66
	900	0.52	366.8	0.37	2.52	-	2.73

scribed by van Bohemen et al. [27]. The dilatation data below 0.2 vol-% martensite fraction was excluded from the fitting to reduce the effect of the observed initial gradual martensite start on the fit, as it was shown by Sourmail and Smanio [28] that the observed gradual start of the martensite transformation can be treated as an effect of thermal gradients and austenite grain size distribution in the dilatation specimen, rather than an intrinsic property of the martensite transformation. The M_s value was determined directly from the least squares fitted Koistinen-Marburger equation.

The microstructure of the steels annealed at 850 °C was examined with optical and scanning electron microscopy. The specimens were sectioned, ground and polished with 0.1 μm colloidal silica used in the final polishing step. Additionally, the optical microscopy specimens were tint etched for 10 s with the Le Pera etchant [29]. The optical microscope used was the Alicona InfiniteFocus G5. Ten micrographs were taken from each specimen at a resolution of 11.4 px/μm and a field of view of 162x162 μm. The phase fractions of martensite and ferrite were determined using the automated intensity thresholding tool in the Fiji open source image analysis software [30]. Carbon extraction replicas were then manufactured from the optical microscopy specimens and subjected to an examination by transmission electron microscopy (TEM) in a Jeol JEM 2010 to determine if any type

of carbides were present in the steels after quenching.

EBSD studies were conducted with a Zeiss Ultra Plus UHR FEG-SEM system fitted with a Nordlys F400 EBSD detector. For the fully austenitized reference sample condition, four maps of 119x82 μm were collected with a step size of 0.3 μm. For each intercritical annealing condition at 850 °C, three sets of 35x24 μm were measured with a step size of 0.05 μm. Grain maps were constructed from the datasets at an angular tolerance of 3 °. Prior to the reconstruction, the intercritical ferrite was excluded using a grain average band slope cutoff, a method used previously [31,32] to succesfully separate ferrite and martensite. The grain map datasets were then processed with the prior austenite reconstruction algorithm.

A script for automated prior austenite reconstruction was written on Matlab® supplemented with the MTEX texture and crystallography analysis toolbox developed by Bachmann et al. [33]. The inflation operator r was set to 1.6 and the threshold value for pruning was set to 0.001. The stochastic matrix T_{G+I} was run through alternating sets of expansion and inflation until convergence. Convergence was determined to have occurred when the difference between the maximum value in each column and the sum of Hadamard squares in each column was smaller than 0.001.

5 The evaluation of the reconstruction algorithm

5.1 Orientation relationship determination

The quality of the orientation relationship determined with the iterative algorithm was assessed on the fully austenitized and quenched reference steel by comparing the iteratively obtained OR against every intergranular misorientation in the dataset and calculating the minimum deviation angle, using Equation 2. The mean of all deviation angles is shown in Table 3, in which a lower value indicates a better fit with the experimental data. There was no angular thresholding to sort the misorientations; instead, all of the misorientations in the set were used for the comparison. In addition, each austenite orientation pixel in the reconstructed dataset was compared to its corresponding martensite orientation, thus obtaining a large dataset of misorientations describing the austenite-martensite orientation relationship. This dataset was used for two things: to calculate a mean value of the austenite-martensite misorientations, resulting in a new OR, and to compare the iteratively obtained OR directly to this dataset. The second row of Table 3 shows the results of these comparisons as the mean deviation angle.

The Kurdjumov-Sachs, Nishiyama-Wasserman and Greninger-Troiano ORs were used to make similar comparisons. The iteratively determined OR has a better average fit value compared to the literature ORs, although the Greninger-Troiano OR comes close. The difference between the iteratively determined OR and the one calculated directly from austenite-martensite misorientations is neglibigle. The

Table 3 The fit between various ORs and the experimental and reconstructed data, shown as the mean angular deviation.

Misorientation dataset	Iter.	Rec.	K-S	N-W	G-T
α'_{exp} - α'_{exp}	3.23	3.22	4.38	7.12	3.46
$\gamma_{rec.}$ - α'_{exp}	2.17	2.17	4.14	5.91	2.37

iteratively determined OR was found to provide a satisfactory match for the experimental data.

5.2 Reconstruction result

A partial EBSD grain map for the reference steel with IPF ND coloring is shown in Figure 2a). The entire dataset contains 5357 grains, from which MCL found 579 discrete clusters. The reconstruction resulted in 196 prior austenite grains (angular threshold 5 degrees). From Figure 2b) it is clear that MCL has oversegmented the graph compared to the final reconstruction result (shown in Figure 2c)).

In Figure 2c), green boundaries indicate twinned austenite grain boundaries. It is expected that these boundaries should follow the traces of the coinciding (111) planes of the twins. However, it is evident from Figure 2 that in several cases the boundaries follow a somewhat jagged line. This is likely a sign of some austenite

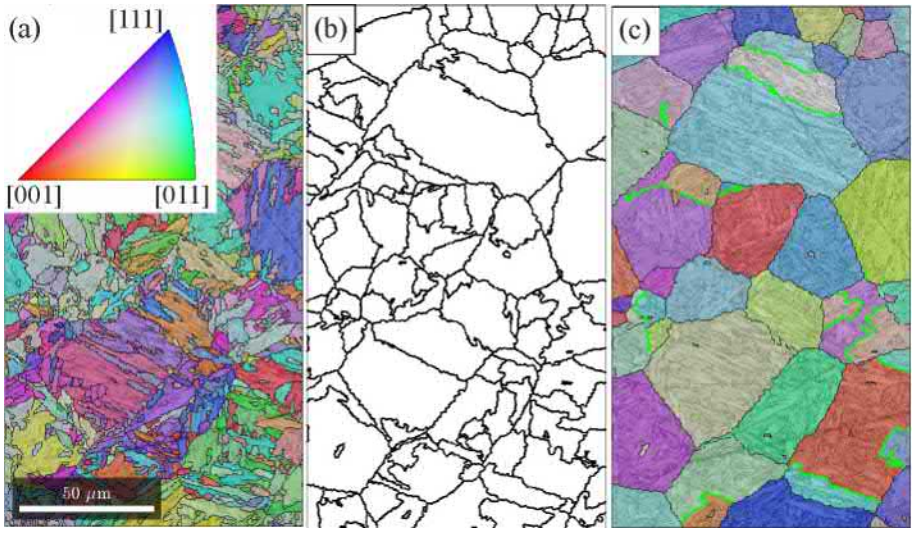

Fig. 2 EBSD band contrast image overlaid with an IPF ND orientation colored grain map. The color key is displayed in the upper left corner of Figure 1a). Reference steel held at 1200 °C for 3 minutes and quenched to RT: a) martensitic EBSD grain map, b) discrete clusters assembled by MCL and c) reconstructed austenite grain map. Highlighted grain boundaries indicate twin boundaries with coincidence site lattice $\Sigma = 3$ equivalence. For colors, please refer to the online version.

orientations misindexed as their twin.

An example of a probable twin misindexation is shown in Figure 3, which shows three reconstructed prior austenite grains. The middle grain (grain 2) shares a twin relationship with its neighbors. The (100) pole figure in Figure 3c) shows the martensite orientations corresponding to the large bottom grain (grain 1). Theoretical martensitic orientations were calculated from the reconstructed austenite orientations of grains 1 and 2 and they are shown as superimposed black (grain 1) and magenta (grain 2) dots in Figure 3c). Careful examination of the pole figure shows the presence of martensite orientations that should be classified to the twin orientation instead. It should be mentioned that following a strict $\Sigma 3$ twin relationship and a strict Kurdjumov-Sachs type orientation relationship, six of the martensite variants shown in Figure 3 should coincide exactly [14,34,35,36]. Evidently, this is not the case here, as shown by the calculated and experimentally

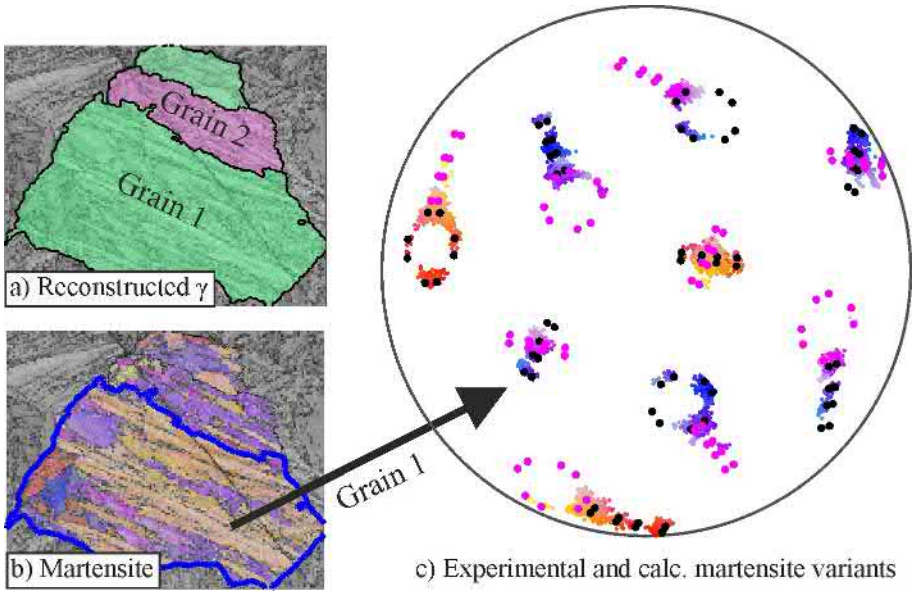

Fig. 3 Cropped orientation map segments showing a) prior austenite grains with IPF TD coloring, and b) corresponding martensite orientations. The (100) pole figure in c) shows the measured martensite orientations from b), along with theoretical martensite variant orientations calculated from the orientations in a). For the IPF color key, refer to Fig. 2a). Consult the online version of the article for references to color.

obtained martensite orientations in Figure 3c). The observed misorientation between reconstructed grains 1 and 2 deviates from $\Sigma 3$ by approximately 1 degree. In addition, it has been shown by Miyamoto et al. [13] that when the experimentally obtained orientation relationship deviates to a significant degree from the K-S OR (as is the case here), the expected overlap of martensite orientations disappears even with an ideal $\Sigma 3$ twinning relationship. In optimal conditions the correct parent orientation may then be calculated from the misorientation between only a pair of orientations [13].

Following this idea, another calculation was made to further study the underlying problems related to twin misindexation. All of the possible misorientations between individual martensite orientation pixels corresponding to the prior austenite grains highlighted in Figure 3a) were compared to each other to determine the symmetry operators C_i and C_j, as in Equation 2. The prior austenite orientations were then calculated for each neighboring $O_{\alpha'}(x_i)$ and $O_{\alpha'}(x_j)$ pair in the following manner:

$$\begin{aligned} O_\gamma(x_i)P_i &= O_{\alpha'}(x_i)(T_{\gamma\to\alpha}C_i)^{-1} \\ O_\gamma(x_j)P_j &= O_{\alpha'}(x_j)(T_{\gamma\to\alpha}C_j)^{-1} \end{aligned} \tag{9}$$

Although the symmetry operators P_i and P_j remain unknown, the left side of Equation 9 should equal crystallographically related solutions of O_γ. Each obtained pair of austenite orientations was compared to each other to verify this. Figure 4a) shows the results of the calculation: a partially reconstructed austenite orientation map calculated from the misorientations between pairs of individual orientation pixels. The presence of an unidentified twin in the lower region of the prior austenite grain (highlighted with a white rectangle) appears to be confirmed by the calculations.

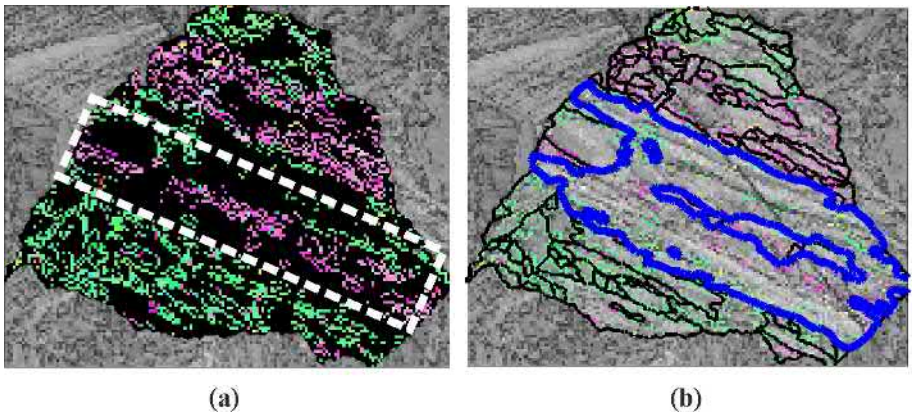

Fig. 4 Austenite orientations with IPF TD coloring (refer to Fig. 1a) for color key), calculated from individual misorientations, with a) a black underlay for emphasis and a highlighted extra twin and b) original martensite grain map overlay. Consult the online version of the article for references to color.

Figure 4b) has been overlaid with the grain boundaries of the initial grain map reconstructed from the martensite orientation map. It is telling that based on the partial reconstruction calculated from individual misorientations, the boundaries of the misidentified twin lie within a single large grain of the initial martensite grain map, outlined blue in the Figure. It is clear that the initial grain reconstruction of the martensite orientation map has failed to differentiate regions with sufficient (lath) accuracy. In this case, the angular threshold was 3 degrees; it appears that some of the low-angle boundary misorientations between individual laths have fallen below this value. It follows that the graph generated from the initial grain map based on misorientation angle thresholding lacks information related to low-angle interlath boundaries. The algorithm described here is therefore unable to segment the map at these locations, resulting in twin misindexation. A logical step towards improving the algorithm would be the incorporation of some other method to generate the initial graph; one such possibility would be to segment the orientation map based on the intermartensitic misorientations identified in the final iteration round of the orientation relationship determination algorithm, possibly combined with a boundary completion algorithm such as ALGrId [37].

6 Results of the intercritical annealed specimens

6.1 Dilatometry results for intercritical annealing

The measured M_s values are shown in Figure 5 for all tested conditions. The curves in Figure 5 show a calculated prediction for M_s versus annealing temperature. The measured temperatures fall well below the predicted values at all annealing temperatures and holding times.

6.2 Prior austenite morphology

The EBSD austenite orientation maps were reconstructed for the DP steels, following the separation of the data into ferrite and martensite by grain average band slope cutoff. Examples of the reconstructed intercritical microstructures are shown in Figure 6. The austenite grains distinguished in the steels have both faceted and smoothly curved interfaces with neighboring ferrite. After 60 minutes, the grains have undergone significant growth. Figure 7 shows the grain size of the reconstructed austenite grains with respect to annealing time, determined through the point-sampled intercept length method demonstrated as suitable for the grain size

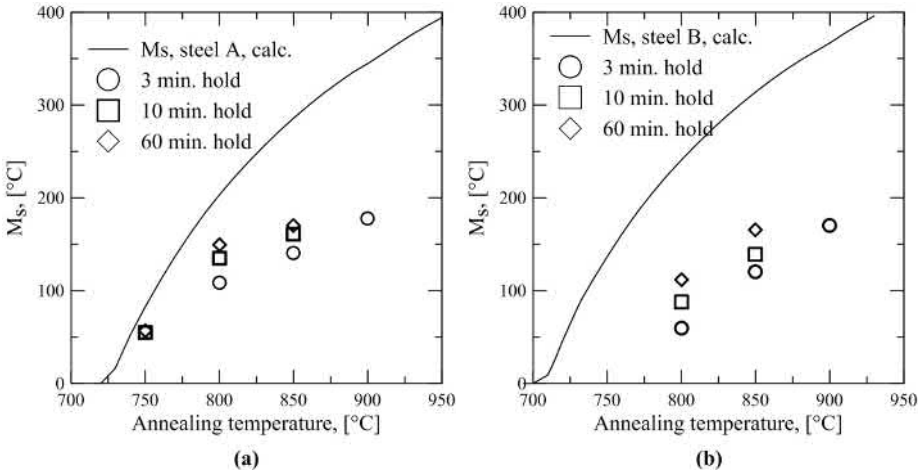

Fig. 5 M_s temperature with respect to annealing temperature for a) steel A and b) steel B.

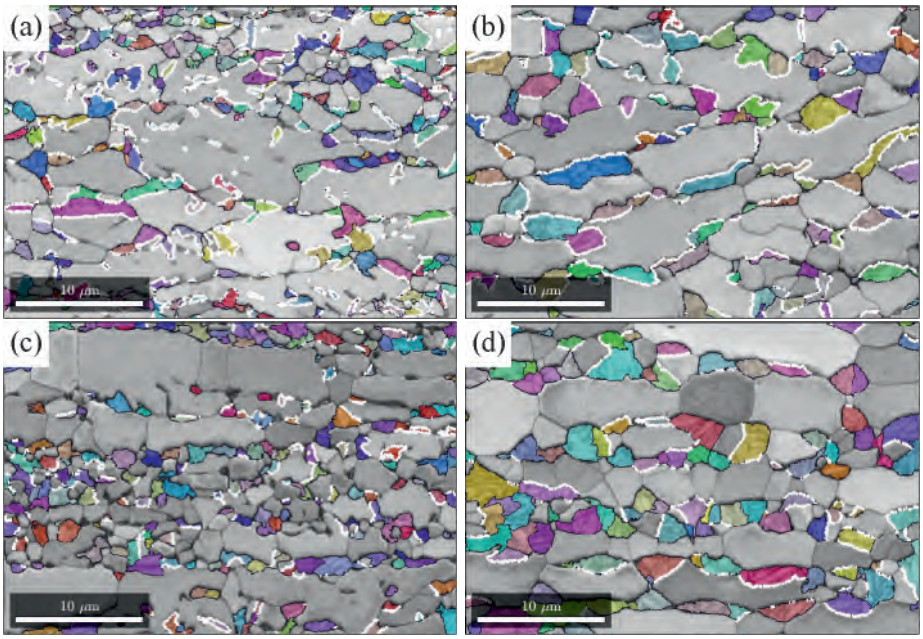

Fig. 6 EBSD band contrast image overlaid with IPF ND orientation coloring for reconstructed austenite (ref. to Fig. 1a) for color key). Steel A: a) 3 minute annealing, b) 60 minute annealing. Steel B: c) 3 minute annealing, d) 60 minute annealing. K-S-type boundary indicated in white. For colors, please refer to the online version.

characterization of complex steel microstructures by Lehto et al. [38] The error bars show the standard deviation of the measured line intercept values.

6.3 Orientation relationships

The average OR between martensite and reconstructed austenite was determined for all of the reconstructed datasets using the iterative procedure described in Section 3, as well as through the direct comparison of the reconstructed austenite and corresponding martensite orientations. In the latter case, the iterative procedure was modified to find a solution for $T_{\gamma\to\alpha}$ using Equation 1, as O_γ was known for each $O_{\alpha'}$ after the reconstruction.

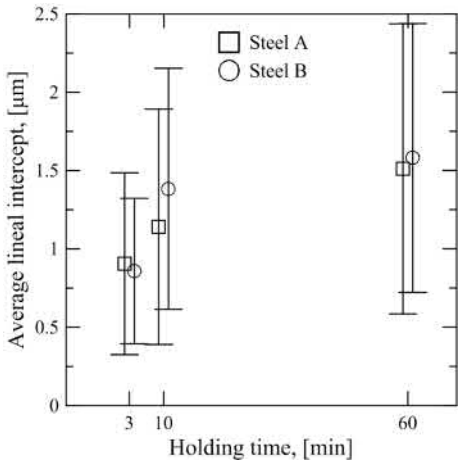

Fig. 7 Reconstructed prior austenite grain size obtained from EBSD maps for the annealing at 850 °C. The data points are staggered on the x axis to improve readability.

Several of the reconstructed austenite grains shared a Kurdjumov-Sachs type grain boundary with neighboring intercritical ferrite. This type of semicoherent boundary was typically associated with a faceted rather than a curved interphase boundary. The exact OR describing this type of boundary was determined with the modified iterative algorithm.

The austenite-martensite OR determined with the iterative algorithm for Steel A annealed for 1 hour at 850 °C is shown in Figure 8a). For this analysis, all of the experimentally found intergranular misorientations were reindexed as the orientation relationship of $(111)\gamma$ and $[\bar{1}01]\gamma$ between $(011)\alpha$ and $[\overline{11}1]\alpha$. Figure 8a) shows a standard stereographic projection for the austenite phase in the middle, with close-up sections of the $[\bar{1}01]\gamma$ and $(111)\gamma$ regions in the sides. Corresponding $(011)\alpha$ and $[\overline{11}1]\alpha$ orientations are overlaid on the close-up regions as contour maps.

The averaged OR is overlaid as a white circle and coincides with the peaks of the contours. $(111)\gamma$ and $[\bar{1}01]\gamma$ are shown to be almost but not exactly parallel with $(011)\alpha$ and $[\overline{11}1]\alpha$. Figure 8b) shows a similar analysis done using the OR determined with the modified iterative method using the misorientations be-

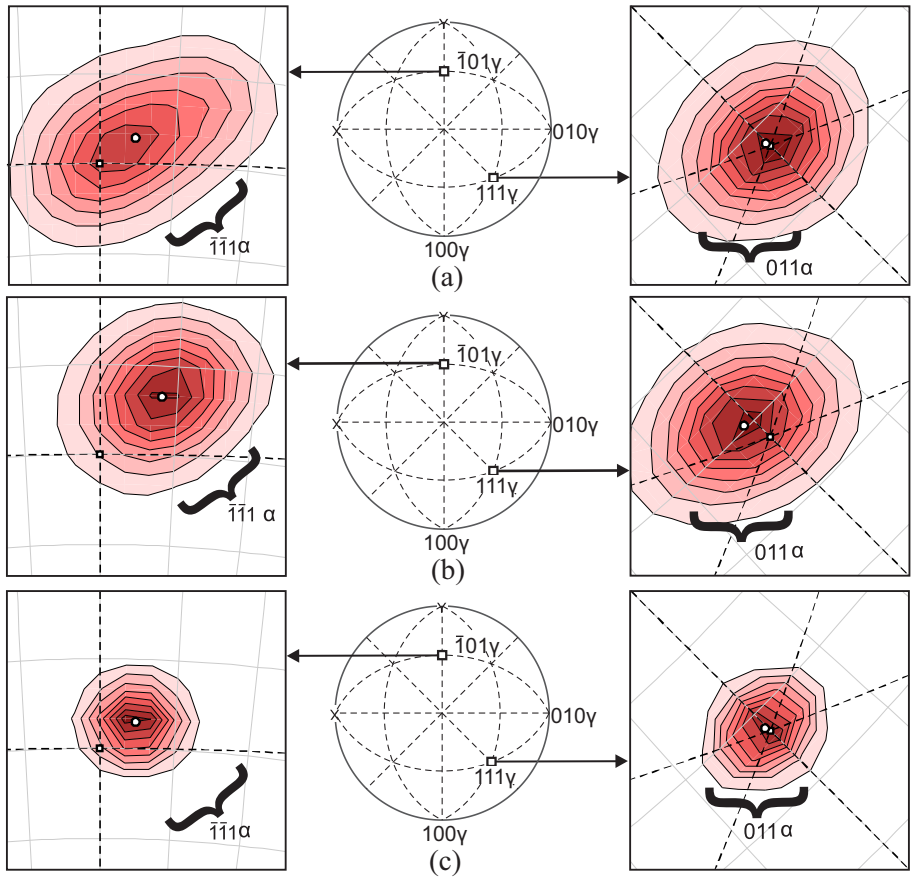

Fig. 8 Examples of the distribution of the orientation relationship between austenite, martensite, and intercritical ferrite for steel A annealed at 850 °C for 60 minutes. Grid spacing in the pole figures is 3 degrees. a) OR determined through boundary misorientation analysis and b) direct comparison between austenite and martensite. c) The orientation relationship between intercritical ferrite and austenite at semicoherent boundaries.

tween reconstructed austenite and corresponding martensite orientations. Figure 8c) shows the OR distribution of the boundaries of reconstructed austenite sharing a K-S type orientation relationship with neighboring intercritical ferrite (the boundaries shown in white in Figure 6). The determined orientation relationships were similar for both steels and invariant with respect to annealing time.

6.4 Martensite morphology and variant formation

Following the reconstruction, a martensite variant indexation number could be determined for each martensitic orientation pixel following the convention of Morito et al. [21], where the variants are divided into groups sharing the same near-parallel close-packed planes: V1-V6, V7-V13, V14-V18 and V19-V23. Table 4 describes the approximate plane and direction parallelisms of each martensitic variant, as well as the corresponding intervariant misorientations calculated from the experimentally obtained orientation relationship for steel A annealed for 1 hr. Figure 9 shows examples of variant distribution in both steels annealed at 850 °C for the annealing times of 3 minutes and 1 hour.

The variant pairing in the steels was studied further by applying the orientation relationship determination algorithm described in Section 3 to each pixel-to-pixel misorientation in the spatially decomposed orientation map, rather than the misorientations between grain average orientations. This increased the data available to the algorithm and allowed the direct calculation of each variant pair boundary length fraction. Each intervariant misorientation was then classified according to the notation described in Table 4. Figure 10 shows the boundary length fractions of each variant pairing. It is clear both from Figure 9 and Figure 10 that within a packet, V1-V2 and V1-V6 type of variant pairing is preferred. On packet boundaries, there is a clear preference toward V1-V16 and V1-V17 types of variant pairings.

A byproduct of the indexation of boundary misorientations was the resolution of block and packet boundaries. Examples of block and packet boundaries are shown in Figure 9, where green boundaries denote block boundaries and red boundaries packet boundaries. The indexed boundaries are in good agreement with the variant numbering. Similarly to the parent austenite, the block and packet

Table 4 24 variants in martensite as defined by Morito et al. [21]. Misorientation axes and angles are shown for the OR measured for steel A annealed for 1 hr.

Variant	**Plane parallel**	**Direction parallel**	**Rotation from Variant 1**	
No.		$[\gamma]\|\|[\alpha']$	**Axis (indexed by martensite)**	**Angle [deg.])**
V1		$[\bar{1}01]\|\|[\bar{1}\bar{1}1]$	-	-
V2		$[\bar{1}01]\|\|[\bar{1}1\bar{1}]$	[-0.5554 0.5332 0.6381]	60.15
V3	$(111)\gamma$	$[01\bar{1}]\|\|[\bar{1}\bar{1}1]$	[-0.0098 0.7000 0.7141]	60.01
V4	$\|\|(011)\alpha'$	$[01\bar{1}]\|\|[\bar{1}1\bar{1}]$	[-0.6322 -0.0000 0.7748]	6.17
V5		$[1\bar{1}0]\|\|[\bar{1}\bar{1}1]$	[-0.7000 0.0098 0.7141]	60.01
V6		$[1\bar{1}0]\|\|[\bar{1}1\bar{1}]$	[-0.7071 0.0054 0.7071]	53.87
V7		$[10\bar{1}]\|\|[\bar{1}\bar{1}1]$	[-0.5922 0.5465 0.5922]	49.71
V8		$[10\bar{1}]\|\|[\bar{1}1\bar{1}]$	[-0.6486 0.1985 0.7348]	11.17
V9	$(1\bar{1}1)\gamma$	$[\bar{1}\bar{1}0]\|\|[\bar{1}\bar{1}1]$	[-0.6486 0.1985 0.7348]	51.28
V10	$\|\|(011)\alpha'$	$[\bar{1}\bar{1}0]\|\|[\bar{1}1\bar{1}]$	[-0.4754 0.5475 0.6886]	49.77
V11		$[011]\|\|[\bar{1}\bar{1}1]$	[-0.4974 0.0641 0.8651]	14.68
V12		$[011]\|\|[\bar{1}1\bar{1}]$	[-0.6556 0.1770 0.7341]	57.33
V13		$[0\bar{1}1]\|\|[\bar{1}\bar{1}1]$	[-0.0641 0.4974 0.8651]	14.68
V14		$[0\bar{1}1]\|\|[\bar{1}1\bar{1}]$	[-0.5475 0.4754 0.6886]	49.77
V15	$(\bar{1}11)\gamma$	$[\bar{1}0\bar{1}]\|\|[\bar{1}\bar{1}1]$	[-0.2373 0.6619 0.7110]	55.59
V16	$\|\|(011)\alpha'$	$[\bar{1}0\bar{1}]\|\|[\bar{1}1\bar{1}]$	[-0.6871 0.2361 0.6871]	18.17
V17		$[110]\|\|[\bar{1}\bar{1}1]$	[-0.6460 0.4067 0.6460]	49.99
V18		$[110]\|\|[\bar{1}1\bar{1}]$	[-0.2709 0.6549 0.7055]	49.67
V19		$[\bar{1}10]\|\|[\bar{1}\bar{1}1]$	[-0.1985 0.6486 0.7348]	51.28
V20		$[\bar{1}10]\|\|[\bar{1}1\bar{1}]$	[-0.1770 0.6556 0.7341]	57.33
V21	$(11\bar{1})\gamma$	$[0\bar{1}\bar{1}]\|\|[\bar{1}\bar{1}1]$	[-0.1477 0.0000 0.9890]	20.43
V22	$\|\|(011)\alpha'$	$[0\bar{1}\bar{1}]\|\|[\bar{1}1\bar{1}]$	[-0.6549 0.2709 0.7055]	49.69
V23		$[101]\|\|[\bar{1}\bar{1}1]$	[-0.6619 0.2373 0.7110]	55.59
V24		$[101]\|\|[\bar{1}1\bar{1}]$	[-0.2605 0.0000 0.9655]	20.77

sizes were determined with the point linear intercept method and are displayed in Figure 11.

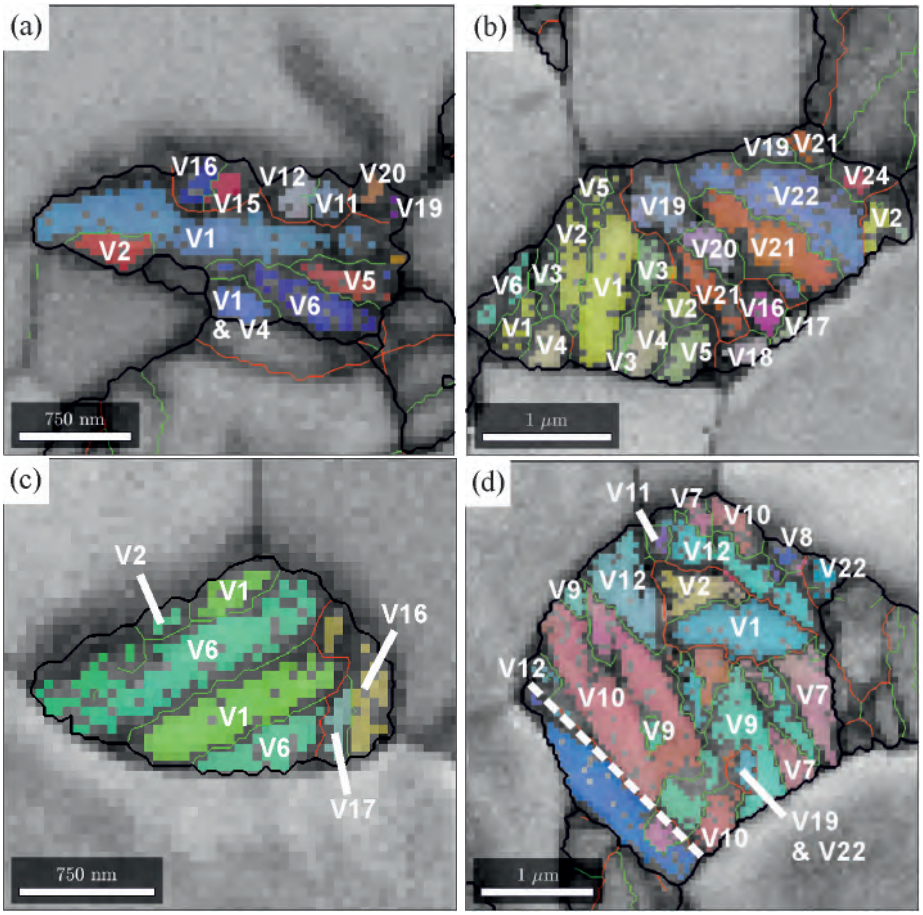

Fig. 9 Examples of martensitic variant distributions in prior austenite grains. Band contrast images with martensite orientations colored in IPF ND coloring (ref. to Fig. 1a) for color key). Red = packet boundaries, green = block boundaries. Steel A: a) 3 minute anneal, b) 1 hr anneal. Steel B: c) 3 minute anneal, d) 1 hr anneal (twin boundary indicated with dashed line). For colors, please refer to the online version.

7 Discussion

7.1 Austenite nucleation, grain growth and crystallography

It has been established that the optimal shape and location for an austenite nucleus is the one that results in the smallest total interfacial free energy [39]. Generally speaking, this means that new grains will preferentially nucleate as abutted spherical caps at grain boundaries. A semicoherent boundary with a well-defined orientation relationship may be created with one of the neighbors, reducing inter-

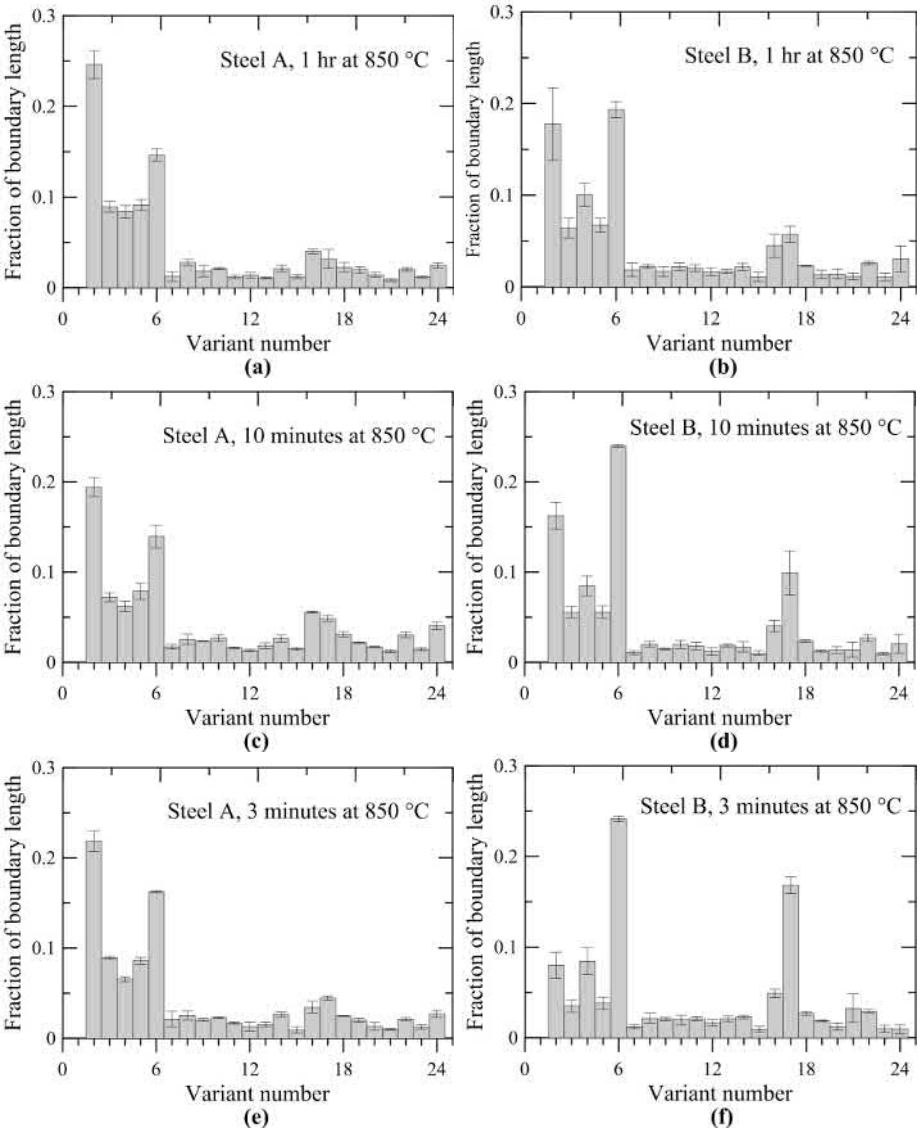

Fig. 10 Variant pairing distributions in the steels A (a), c) and e)) and B (b), d) and e)) for the annealing times of: a) and b) 1 hr, c) and d) 10 minutes and e) and f) 3 minutes reported as fraction of total boundary length of each variant pair.

514 facial energy and, consequently, resulting in texture inheritance from one phase
515 to another. Further reductions to activation energy can be gained by nucleation
516 at grain edges and corners, where the potential removal of a high-energy defect

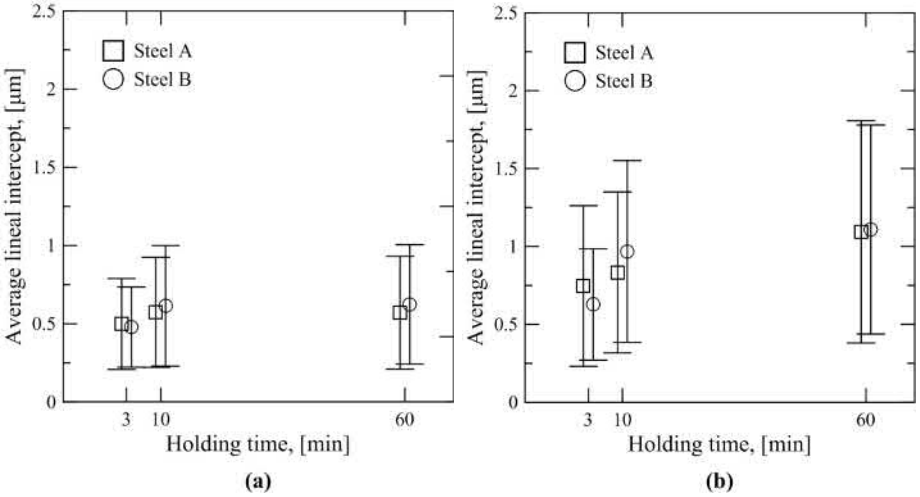

Fig. 11 Martensite a) block and b) packet size obtained from EBSD maps for the annealing at 850 °C. The data points are staggered on the x axis to improve readability.

reduces the energy barrier for nucleation.

Nearly all of the reconstructed prior austenite grains nucleated at grain boundaries (see Figure 6) were found to share a Kurdjumov-Sachs type orientation relationship with at least one of its ferritic neighbors. Most of the prior austenite had nucleated at the grain boundaries, edges or corners of the recrystallized ferrite grains, likely after carbide dissolution had provided a carbon-rich volume preferential to austenite nucleation. A small amount of austenite had also nucleated at defects inside ferrite grains. Commonly these had a K-S type OR with the surrounding ferrite and an elongated shape, the long axis being parallel with a {011} plane in ferrite and a {111} plane in austenite.

Grain boundary nucleation with a single semicoherent interface was most common in steel A, where the ferrite grain size distribution is unimodal. In the case of steel B, the distribution of intercritical ferrite size is bimodal, providing more high-energy nucleation sites (grain edges and corners) for austenite. This results in a lesser need for semicoherent boundaries to lower the interfacial energy, and

thus a smaller amount of grains sharing a semicoherent boundary with neighboring austenite. The degree of texture inheritance from recrystallized ferrite is thus reduced in steel B. The average area fraction of austenite grains with no orientation relationship to neighboring ferrite increased from approximately 15 % (steel A) to approximately 40 % (steel B) with no effect from the annealing time. This implies that by providing an ample amount of high-energy nucleation sites for austenite (for example by reducing recrystallized ferrite grain size), the texture inheritance from one manufacturing stage to another could be reduced. This is perhaps not so important for DP steels, in which recrystallized ferrite is the phase that accommodates most of the deformation during later shaping processes. However, non-textured austenite could be useful in operations where the nucleation and growth of austenite proceeds to full austenitization, followed by deformation while in the austenitic stage.

Figure 7 shows that the growth rate of austenite is initially rapid, slowing down considerably at extended annealing times. This is consistent with previous findings [4,5]. For austenite nucleated at grain boundaries, the growth of the austenite grain was typically accomplished by an increase of curvature in the direction of the ferrite grain that did not share an ordered semicoherent boundary with the neighboring austenite. In most cases, the semicoherent boundary retained its faceted shape even after an extended annealing time. It should be mentioned that the observation of increased curvature is based on the examination of data on a 2D plane. In any case, based on the observed growth behavior both in terms of austenite grain size and increased curvature on a 2D plane, the primary growth mechanism of the austenite appears to be diffusion across an incoherent interphase boundary. It is possible that the diffusion of aluminum from austenite to ferrite becomes the controlling factor in austenite growth: the volume ahead of the transformation front is enriched with ferrite-stabilizing aluminum, which must diffuse further away from the interface before the transformation can continue. The slow

growth of the austenite phase has been attributed to this type of substitutional diffusion of heavier alloying elements (such as Mn or Cr) in other works as well [4, 9, 40].

A deviation was observed between the results for the austenite-martensite OR generated by the iterative boundary misorientation analysis and by direct austenite-martensite comparison. From Figure 8a, the OR determined iteratively from grain pair misorientations suggests a nearly perfect parallelism between $(011)\alpha'$ and $(111)\gamma$, while the OR determined through the direct comparison of reconstructed austenite and corresponding martensite (Figure 8b) suggests that the martensite close-packed planes deviate from those of austenite by approximately a degree on average. This difference between results is explained by the fact that the iterative OR determination algorithm characterizes the misorientations between martensitic blocks and packets, which are composed of martensitic laths. As shown earlier by Miyamoto et al. [41], during transformation, the austenitic matrix surrounding the newly formed martensitic laths has deformed plastically and elastically to accommodate the shape change. When another martensite lath forms immediately next to the initial lath, its orientation must accommodate the deformed austenite. It stands to reason that the orientation relationship measured from the average misorientation between these kinds of neighboring laths will differ from the orientation relationship between the formed martensite and the local austenite orientation. In the case of direct comparison between reconstructed austenite and martensite orientations, this is avoided. The results suggest that while iterative boundary misorientation analysis provides a good first approximation for reconstruction purposes, accurate orientation relationship studies preferentially require direct comparison between the reconstructed austenite and martensite orientations.

7.2 Martensite transformation

The EBSD studies showed that the microstructure consisted of intercritical ferrite and an arrangement of smaller ferrite laths that could be reconstructed into prior austenite. Combined with the results dilatometric studies, which indicated a phase change at a relatively low temperature (below 200 °C), it is likely that the lath arrangements are untempered martensite. This was supported by the TEM studies on the carbon replicas. The only type of carbides found in these studies were a small amount of approximately spherical niobium carbides ranging from 5 to 20 nm in diameter. The orientation relationship between the carbides and the surrounding ferrite could not be determined, as the surrounding metallic matrix had fully dissolved in the replica. Considering the relatively small molar fraction of niobium in the experimental alloys, it is likely that the majority of carbon resides in solution in the untempered martensite.

The phase fractions of intercritical ferrite and austenite in steel A and steel B annealed at 850 °C for the holding time of 60 minutes were estimated from optical micrographs. These are shown in Figure 12. For shorter holding times, reliable phase fraction analyses could not be made via optical microscopy due to the small austenite grain size and optical microscopy resolution limitations.

For correlation, phase fractions were also extrapolated by comparison of the measured M_s values with the curves shown in Figure 5. Before comparison, M_s was offset with the correction for austenite grain size determined with Equation 10 by Yang and Bhadeshia [42]:

$$M_s^0 - T = \frac{1}{b} ln[\frac{1}{aV_\gamma}\{e^{-\frac{ln(1-f)}{m}} - 1\} + 1] \quad (10)$$

In Equation 10, a and b are empirically determined fitting constants with values 1 mm^{-3} and 0.2689, respectively. $f = 0.01$ represents the first detectable fraction

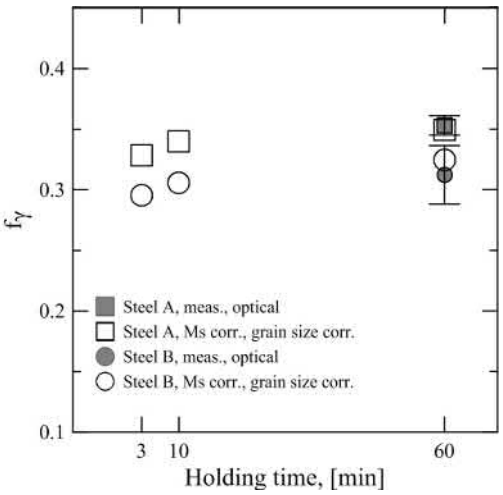

Fig. 12 Phase fractions obtained directly through optical metallography and extrapolation from measured M_s.

of martensite and $m = 0.05$ the aspect ratio of a martensite lens. V_γ is the volume of the parent austenite grain and is approximated by L_γ^3, L_γ representing the grain size of the parent austenite. L_γ was substituted with the average measured linear intercept value from the reconstructed parent austenite orientation maps. The grain sizes observed here resulted in a calculated decrease of M_s in the range of 66-75 °C.

The extrapolated values correlate with the austenite fractions measured directly from optical micrographs. Thus, it is a likely explanation that the low measured M_s values are the result of a combination of two factors: low fractions of intercritical austenite prior to the onset of martensite transformation as well as the small prior austenite grain size.

There are two possible explanations for the low intercritical austenite phase fraction. Either the balance of phases has changed during cooling to room temperature, or the steel alloy has not had sufficient time to achieve equilibrium during annealing. The change of phase fractions during cooling would be facilitated by the Widmanstätten growth of ferrite into austenite, diffusion-aided interfacial

635 migration, or the formation of bainite. No clear ferritic Widmanstätten-type pro-
636 trusions were found in the microstructure, leaving the interfacial growth of ferrite
637 into austenite or bainite formation. Analysis of the dilatation curves did not reveal
638 any clear evidence of bainite or ferrite transformations.
639

640 The evidence obtained here suggests that the first explanation is correct: slow,
641 diffusion-aided growth of the austenite phase during annealing has not allowed the
642 austenite phase to reach equilibrium even after extended annealing times. How-
643 ever, the interpretation of the cooling curves in the high-temperature regime where
644 diffusion-aided phase transformation might occur is not straightforward, so ferrite
645 interfacial growth or limited bainite formation during cooling cannot be completely
646 ruled out.
647

648 The main variant pairs formed in the steels studied here were V1-V2 and V1-
649 V6. V1-V4 type martensite variant pairing is preferred in low-carbon martensite,
650 as shown by Stormvinter et al. [22] and Morito et al. [21]. Such variant pairing
651 was not common in the steels studied here. Rather, the morphology and crystal-
652 lography of the martensite closely follows earlier observations for lath martensite
653 formed in a Fe-0.6C [21] or Fe-0.7C [22] steel, in which V1-V4 type sub-block
654 boundaries were found to be either nearly completely absent [21] or not nearly
655 as common [22]. This variant pairing behavior was attributed to a greater need
656 (compared to low-carbon lath martensite) for plastic self-accommodation result-
657 ing from high carbon content and (consequent) low transformation temperature.
658 Based on the experimental evidence, it is likely that the same factors apply for
659 the steels studied here. The carbon content in austenite is high and the grain
660 size has remained small as the result of intercritical annealing, resulting in a low
661 observed M_s and thus a high critical driving force necessary for the transformation.
662

There is a preference for V1-V16/V17 type of variant pairing across packet boundaries. The tendency for such boundaries was noted to increase with carbon content by Stormvinter et al. [22]. There is a notable decrease in V1-V2 and an increase in V1-V6 boundaries for steel B at shorter annealing times, which is accompanied by an increase in V1-V17 type packet boundaries. V1,V6,V16,V17 belong to the same plate group, noted to form in burst fashion as the result of autocatalytic nucleation in high-nickel plate martensite [43, 44] and high-carbon steel [22]. It is possible that at shorter annealing times, steel B is shifting towards the generation of plate martensite. At the very least, there is a clear preference towards the generation of variants belonging to the same plate group.

8 Conclusions

1. Markov clustering combined with automatic iterative orientation relationship determination can be used to succesfully reconstruct austenite orientation maps in both fully austenitized and intercritically annealed microstructures.
2. Austenite has a tendency to nucleate at grain edges and corners, when enough of these high-energy nucleation sites are provided. In these cases the need for a semicoherent interface with neighboring ferrite is reduced. When ferrite grain size is large, austenite may nucleate with a semicoherent K-S type interface with one neighbor and an incoherent interface with another. Austenite growth may occur most rapidly via diffusion in the direction of the incoherent boundary.
3. The orientation relationship at ferrite-austenite semicoherent boundaries deviates slightly from Kurdjumov-Sachs, with approximately one degree deviation between $(011)\gamma$ and $[\overline{1}\overline{1}1]\alpha$ (as indicated by the mean of the orientation relationships determined from the observed K-S type boundaries).
4. It was observed that for the intercritically annealed steels studied here, there is a small but systematic difference in the orientation relationships deter-

mined from boundary misorientations and those determined from martensite-reconstructed austenite misorientations.

5. The low M_s temperatures are explained by a combination of phase fraction inequilibrium at the onset of cooling and small austenite grain size.
6. It was observed that in an intercritically annealed condition, the martensite consists of single-variant blocks preferentially forming V1-V2 or V1-V6 type variant pairs in a packet. A preference was also observed towards the formation of variants belonging to the same plate group.

An interesting possibility is raised by the tendency of austenite in steel B to nucleate at grain edges and corners, when ferrite grain size is sufficiently small. In these cases, the crystallographic orientation of the austenite is random and there is no texture inheritance from the neighboring recrystallized ferrite. By providing a large amount of high-energy nucleation sites for austenite, it may become possible to reduce the inheritance of cold rolled texture from one manufacturing stage to another, resulting in a more isotropic material.

9 Acknowledgements

This work was supported by the Graduate School CE Tampere, the Walter Ahlström Foundation, KAUTE Foundation, TES Foundation and the Tampere University of Technology. The Advanced Steel Processing and Products Research Center in the Colorado School of Mines is gratefully acknowledged for providing the use of the TA DIL805 dilatometer for these studies.

The reconstruction algorithm and associated Matlab® script presented here is made freely available and can be obtained by request from the corresponding author or from the web address: `https://github.com/nyyssont/parent_austenite_reconstruction`

References

1. S. van Dongen, *Graph Clustering by Flow Simulation*, Ph.D. thesis, University of Utrecht, 2000.
2. T. Nyyssönen, M. Isakov, P. Peura, and V.-T. Kuokkala, *Metall. Mater. Trans. A*, 2016, vol. 47 (6), pp. 2587–2590.
3. G. Kurdjumov, *J. Iron Steel Inst., London*, 1960, vol. 195, p. 26.
4. C. I. Garcia and A. J. Deardo, *Metall. Mater. Trans. A*, 1981, vol. 12 (3), pp. 521–530.
5. D. Shtansky, K. Nakai, and Y. Ohmori, *Acta Mater.*, 1999, vol. 47 (9), pp. 2619–2632.
6. L. Ryde, J. Hagström, and W. B. Hutchinson, *Mater. Sci. Forum*, 2007, vol. 550, pp. 321–326.
7. Z.-D. Li, G. Miyamoto, Z.-G. Yang, and T. Furuhara, *Scr. Mater.*, 2009, vol. 60 (7), pp. 485–488.
8. D. P. Datta and A. M. Gokhale, *Metall. Mater. Trans. A*, 1981, vol. 12 (3), pp. 443–450.
9. G. R. Speich, V. A. Demarest, and R. L. Miller, *Metall. Mater. Trans. A*, 1981, vol. 12 (8), pp. 1419–1428.
10. M. M. Souza, J. R. C. Guimarães, and K. K. Chawla, *Metall. Mater. Trans. A*, 1982, vol. 13 (4), pp. 575–579.
11. D. Z. Yang, E. L. Brown, D. K. Matlock, and G. Krauss, *Metall. Mater. Trans. A*, 1985, vol. 16 (8), pp. 1385–1392.
12. C. Cayron, B. Artaud, and L. Briottet, *Mater. Charact.*, 2006, vol. 57 (4-5), pp. 386–401.
13. G. Miyamoto, N. Iwata, N. Takayama, and T. Furuhara, *Acta Mater.*, 2010, vol. 58 (19), pp. 6393–6403.
14. L. Germain, N. Gey, R. Mercier, P. Blaineau, and M. Humbert, *Acta Mater.*, 2012, vol. 60 (11), pp. 4551–4562.
15. M. Abbasi, D.-I. Kim, T. W. Nelson, and M. Abbasi, *Mater. Charact.*, 2014, vol. 95, pp. 219–231.
16. N. Bernier, L. Bracke, L. Malet, and S. Godet, *Mater. Charact.*, 2014, vol. 89, pp. 23–32.
17. M. Humbert, P. Blaineau, L. Germain, and N. Gey, *Scr. Mater.*, 2011, vol. 64 (2), pp. 114–117.
18. M. Humbert, L. Germain, N. Gey, and E. Boucard, *Acta Mater.*, 2015, vol. 82, pp. 137–144.
19. C. Cayron, *Mater. Charact.*, 2014, vol. 94, pp. 93–110.
20. E. Gomes and L. A. I. Kestens, *IOP Conference Series: Materials Science and Engineering*, 2015, vol. 82 (1), p. 012059.
21. S. Morito, H. Tanaka, R. Konishi, T. Furuhara, and T. Maki, *Acta Mater.*, 2003, vol. 51 (6), pp. 1789–1799.
22. A. Stormvinter, G. Miyamoto, T. Furuhara, P. Hedström, and A. Borgenstam, *Acta Mater.*, 2012, vol. 60 (20), pp. 7265–7274.

754 23. M. Abbasi, T. W. Nelson, C. D. Sorensen, and L. Wei, *Mater. Charact.*, 2012, vol. 66, pp.
755 1–8.
756 24. N. Saunders, U. K. Z. Guo, X. Li, A. P. Miodownik, and J. P. Schillé, *JOM*, 2003,
757 vol. 55 (12), pp. 60–65.
758 25. H. K. D. H. Bhadeshia, *Met. Sci.*, 1981, vol. 15 (4), pp. 175–177.
759 26. D. P. Koistinen and R. E. Marburger, *Acta Metall.*, 1959, vol. 7, pp. 59–60.
760 27. S. van Bohemen, M. Santofimia, and J. Sietsma, *Scr. Mater.*, 2008, vol. 58 (6), pp. 488 –
761 491.
762 28. T. Sourmail and V. Smanio, *Mater. Sci. Technol.*, 2013, vol. 29 (7), pp. 883–888.
763 29. F. LePera, *Metallography*, 1979, vol. 12 (3), pp. 263 – 268.
764 30. J. Schindelin, I. Arganda-Carreras, E. Frise, V. Kaynig, M. Longair, T. Pietzsch,
765 S. Preibisch, C. Rueden, S. Saalfeld, B. Schmid, J.-Y. Tinevez, D. White, V. Hartenstein,
766 K. Eliceiri, P. Tomancak, and A. Cardona, *Nat. Methods*, 2012, vol. 9, p. 676.
767 31. L. Ryde, *Mater. Sci. Technol.*, 2006, vol. 22 (11), pp. 1297–1306.
768 32. G. Thewlis, *Mater. Sci. Technol.*, 2004, vol. 20 (2), pp. 143–160.
769 33. F. Bachmann, R. Hielscher, and H. Schaeben, *Solid State Phenom.*, 2010, vol. 160, pp.
770 63–68.
771 34. T. Song and B. C. De Cooman, *Metall. Mater. Trans. A*, 2013, vol. 44 (4), pp. 1686–1705.
772 35. M. Abbasi, T. W. Nelson, and C. D. Sorensen, *J. Appl. Crystallogr.*, 2013, vol. 46 (3), pp.
773 716–725.
774 36. S. Cluff, E. Homer, T. Nelson, R. Song, and D. Fullwood, *IOP Conference Series: Materials*
775 *Science and Engineering*, 2018, vol. 375 (1), p. 012012.
776 37. L. Germain, D. Kratsch, M. Salib, and N. Gey, *Mater. Charact.*, 2014, vol. 98, pp. 66–72.
777 38. P. Lehto, J. Romanoff, H. Remes, and T. Sarikka, *Weld. World*, 2016, vol. 60 (4), pp.
778 673–688.
779 39. J. W. Cahn, *Acta Metall.*, 1956, vol. 4 (6), pp. 572 – 575.
780 40. E. Navara and R. Harrysson, *Scr. Metall.*, 1984, vol. 18 (6), pp. 605 – 610.
781 41. G. Miyamoto, A. Shibata, T. Maki, and T. Furuhara, *Acta Mater.*, 2009, vol. 57 (4), pp.
782 1120–1131.
783 42. H. Yang and H. K. D. H. Bhadeshia, *Scr. Mater.*, 2009, vol. 60 (7), pp. 493–495.
784 43. J. Bokros and E. Parker, *Acta Metall.*, 1963, vol. 11 (12), pp. 1291 – 1301.
785 44. H. Okamoto, O. Muneo, and I. Tamura, *Trans. Jpn. Inst. Met.*, 1978, vol. 19 (12), pp.
786 674–684.